High repetition rate relativistic laser–solid–plasma interaction platform featuring simultaneous particle and radiation detection

Jaismeen Kaur, Marie Ouillé, Dan Levy, Louis Daniault, Axel Robbes, Neil Zaïm, Alessandro Flacco, Eyal Kroupp, Victor Malka, Stefan Haessler, et al.

High repetition rate relativistic laser-solid-plasma interaction platform featuring simultaneous particle and radiation detection

Jaismeen Kaur,[1, a)] Marie Ouillé,[1, 2] Dan Levy,[3] Louis Daniault,[1] Axel Robbes,[1] Neil Zaïm,[1] Alessandro Flacco,[1] Eyal Kroupp,[3] Victor Malka,[3] Stefan Haessler,[1] and Rodrigo Lopez-Martens[1]

[1)]*Laboratoire d'Optique Appliquée, Institut Polytechnique de Paris, ENSTA-Paris, Ecole Polytechnique, CNRS, 91120 Palaiseau, France*

[2)]*Ardop Engineering, Cité de la Photonique, 11 Avenue de la Canteranne, Bât. Pléione, 33600 Pessac, France*

[3)]*Department of Physics of Complex Systems, Weizmann Institute of Science, Rehovot 76100, Israel*

(Dated: 26 October 2023)

We report on a uniquely designed high repetition rate relativistic laser-solid-plasma interaction platform, featuring the first simultaneous measurement of emitted high-order harmonics, relativistic electrons, and low divergence proton beams. This versatile setup enables detailed parametric studies of the particle and radiation spatio-spectral beam properties for a wide range of controlled interaction conditions, such as pulse duration and plasma density gradient. Its array of complementary diagnostics unlocks the potential to unravel interdependencies among the observables, and should aid in further understanding the complex collective dynamics at play during laser-plasma interactions, and in optimizing the secondary beam properties for applications.

I. INTRODUCTION

When an intense femtosecond laser pulse is tightly focused on an optically polished solid surface, it generates a thin layer of surface plasma with near-solid density, which becomes highly reflective for the incident laser light and is therefore often called a "plasma mirror" (PM)[1]. Progress in high-power laser technology going back almost two decades, in particular the generation of ultra-short laser pulses with high temporal contrast[2–4], has enabled the exposure of PMs to peak electric field amplitudes that can drive relativistic plasma electron motion. For typical Titanium:Sapphire (Ti:Sa) lasers emitting around a central wavelength λ_0 = 800 nm, this occurs for peak focused intensities $I_0 > 10^{18}$ W/cm^2 or normalized vector potentials $a_0 = \sqrt{I_0\,[\mathrm{W/cm^2}]\;\lambda_0^2\,[\mu m^2]/1.37\times10^{18}} > 1$.

Both in this so-called relativistic regime, and in the sub-relativistic regime with $a_0 \sim 0.1$, the laser drives complex plasma dynamics that comprise a multitude of phenomena with associated interaction products. These are *(i)* the reflected light, whose frequency content can be vastly increased, both downwards into the THz-region[5] and upwards via high-order harmonic generation (HHG)[6], *(ii)* fast electron bunches[7], and *(iii)* energetic ion beams[8]. This makes PMs potentially interesting sources of ultrashort energetic particle and radiation beams for applications.

However, the majority of laser-plasma beamlines rely on 100 TW-class or even PW-class laser systems, limited to low repetition rates (0.1 - 10 Hz), rendering the generated particle and radiation beams unsuitable for many applications, like extreme ultra-violet (XUV) imaging[9], nuclear physics[10], biomedical applications[11], and ultrafast electron diffraction. Over the past few years, considerable research efforts have been devoted to increasing the laser repetition rate to the kHz range and engineering suitable targets, in order to improve the average brightness and flux of the secondary emissions. High repetition rate generation and detection makes it feasible to collect large data sets to perform statistical studies while scanning a

[a)]Electronic mail: jaismeen.kaur@ensta-paris.fr

high-dimensional parameter space in a reasonable time, also opening the possibility of closed-loop automated optimizations[12].

Thus far, most studies of laser-driven PMs have focused their attention and diagnostics on a single of these observables, thus leaving potential correlations in the dark. Recently, measurements of both HHG and electrons from either successive[13,14] or simultaneous acquisitions[15,16] have been reported. These multiple diagnostics have proven to provide a fine in-situ probe into the collective plasma dynamics, revealing correlations between observables that helped deciphering the rich underlying nonlinear plasma dynamics.

Here, we report on a uniquely designed high-repetition rate laser-plasma interaction platform, capable of simultaneously detecting all three emissions from a well-controlled laser-driven PM: light (HHG), electrons, and protons. Their simultaneous measurement enables us to observe correlations between the signals whilst ensuring identical interaction conditions on-target. At constant driving pulse energy and focused spatial beam distribution, we can vary the driving pulse duration between 4 fs, and 1.5 ps, thus scanning over a wide range of intensities $I \sim 10^{16} - 10^{19}$ W/cm^2 and transitioning from the sub-relativistic to the relativistic regime. The plasma-density gradient on the solid-target surface is controlled and characterized, and is another crucial interaction parameter[16–18] that can be varied.

This platform is the most recent evolution of our setup, whose previous evolutionary stages have lead to some earlier publications by our group:

– The paper introducing the SDI method[19], which we extend here in sections III C, III D and IV A by specifying the data analysis, and discussing the involved assumptions in detail, and by presenting an experimental validation for different pulse durations.

– Two papers reporting only on the ion-signal[8,20], which we extend here in section IV B by measuring and discussing the correlation of proton acceleration with HHG from coherent-wake-emission[21].

– A paper focusing on laser-wakefield acceleration of electrons in long plasma density gradients[22], which we extend here in section IV C by showing the measured energy of the electrons and discussing their anti-correlation with HHG.

– Two papers featuring simultaneous detection of HHG and electrons, in sub-relativistic[15] and relativistic[16] interaction conditions, which we extend here in section IV B by showing measured electron energies and by including simultaneously measured ion spectra.

II. EXPERIMENTAL OBSERVABLES

(i) HHG extends into the XUV and even up to the X-ray[23] spectral ranges and corresponds to a train of attosecond pulses in the time domain[6,24,25]. Two main generation mechanisms have been identified in simulations and experiments: coherent wake emission (CWE)[21] and the relativistic oscillating mirror (ROM)[26,27]. In CWE, the laser field injects vacuum-heated so-called "Brunel" electrons[28] from the surface into the bulk of the plasma, forming a propagating electron density peak which excites plasma oscillations in its wake, finally leading to HHG. CWE is a ubiquitous mechanism in all HHG experiments on PMs[21] and is efficient even at intensities as low as $I \sim 10^{15}$ W/cm^2. ROM only comes into play at relativistic intensities, where the PM surface itself begins to oscillate at relativistic velocities, leading to a periodic frequency upshifting of the reflected light, resulting in HHG. In the relativistic regime, it is important to take electron motion into more detailed account, as in the more advanced relativistic electron spring[29] and coherent synchrotron emission[30–33] models. The relative contributions of relativistic HHG (RHHG) and CWE to the total emission depends mainly on the incident laser intensity[6,33] and the plasma gradient scale length L_g[18]. These two HHG families are clearly distinguishable experimentally through their different phase properties[25,34–36], and intensity dependence[16,21].

(ii) Ultrashort (relativistic) electron bunches are emitted from PMs in different acceleration regimes depending on the plasma conditions. For relatively long density gradients ($L_g > \lambda_0$), electrons are accelerated to multi-MeV energies by a laser wakefield produced inside the underdense part of the plasma density gradient, a process which is only observed with few-cycle driving pulses[22]. For sharper density gradients ($L_g \ll \lambda_0$), electrons ejected out

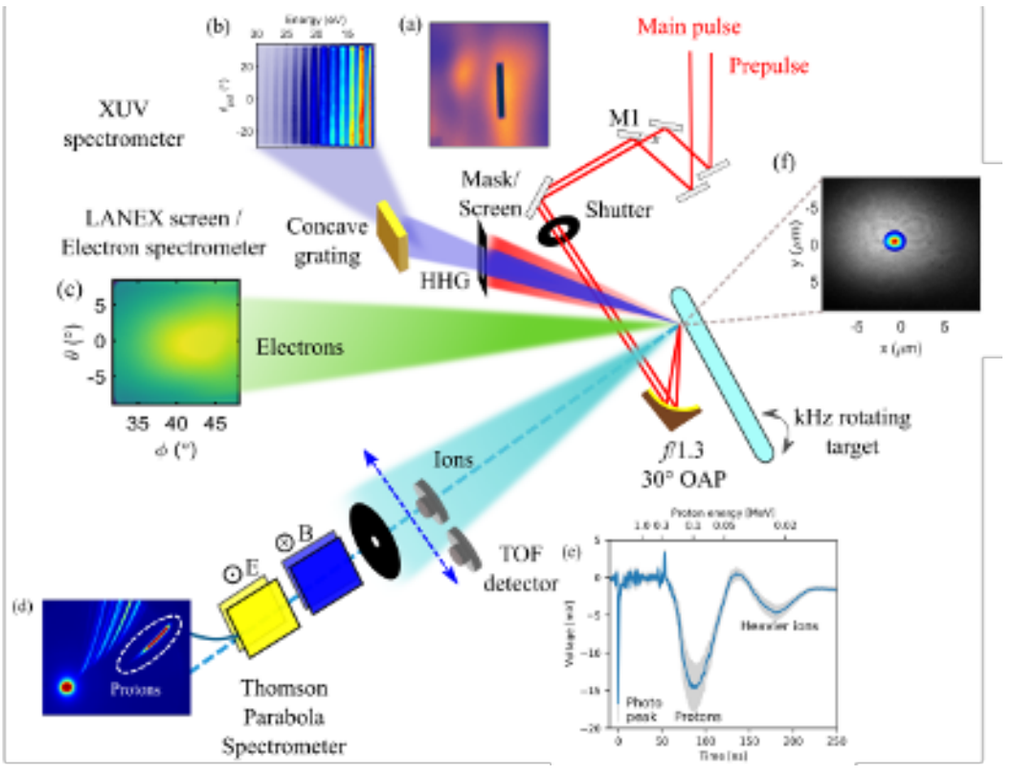

FIG. 1. Experimental set-up for simultaneous detection of HHG, electrons, and protons emitted from a relativistic PM prepared by a weak Pre-pulse and driven by an intense Main pulse. (a) Reflected laser near-field, (b) HHG spectrograph, (c) spatial electron beam profile, (d) parabolic ion tracks, and (e) ion TOF trace are the typically recorded images by the respective diagnostics. (f) On-target Pre-pulse (greyscale) and Main pulse (color scale) spatial beam profiles. M1: Holey mirror

of the plasma surface can co-propagate with the reflected laser field in vacuum and subsequently gain large amounts of energy by vacuum laser acceleration[7]. The energy and charge of the electron beam emitted in this regime have been found to be correlated to RHHG emission[13,16,37] and anti-correlated to CWE[15].

(iii) Ion acceleration from solid-density plasmas has mostly been studied on the beams emitted from the backside of thin targets (in transmission) through the well-known target normal sheath acceleration (TNSA) mechanism[38], which proceeds well after the driving laser pulse has passed. TNSA-based ion sources show large beam divergences, varying from 10° to 30° depending on the driving laser and target parameters[39,40]. Often, additional collimation devices and special target geometries[38,41], along with complicated target fabrication and handling are required to keep the beam collimated. However, in the case of front-side ion acceleration, a different acceleration mechanism driven by Brunel electrons has been found to be more efficient than TNSA for the steepest plasma density gradients[8,42]. Acceleration takes place during the time of interaction of the laser pulse with the plasma and results in extremely low-divergence proton beams[20]. Such exceptional beam properties, useful for numerous potential applications[43,44] from a fairly simple target geometry warrants further exploration of this particular acceleration regime.

III. EXPERIMENTAL SETUP

A. Driving pulses

The experiments were carried out in the *Salle Noire* laser facility at Laboratoire d'Optique Appliquée (LOA), delivering waveform-controlled, up to 2.5 mJ on-target, high-temporal contrast ($> 10^{10}$@10 ps) laser pulses, centered around $\lambda_0 = 780$ nm, with tunable pulse duration from 27 fs to sub-4 fs[45]. While maintaining the same on-target fluence (same energy contained within the same focal area), the laser pulses can also be stretched up to 1.5 ps by adding group delay dispersion using an acoustic-optic programmable dispersion filter (*Dazzler, Fastlite*) integrated into the laser chain. A schematic layout of the experimental set-up is illustrated in figure 1. Under vacuum, the p-polarised Main pulses are focused by an f/1.3 28° off-axis parabolic (OAP) mirror (effective focal length $f = 54.4$ mm) onto a rotating, thick fused optical grade silica target at an incidence angle of $\theta_i = 55°$, to a ≈ 1.8 μm FWHM spot.

B. Solid target and shot sequence

A rotating target positioner refreshes the target surface at kHz repetition rate with precise control over shooting position and rotation speed, maintaining adequate shot spacing between consecutive laser shots[46]. To ensure identical shot-to-shot interaction conditions, the target surface is aligned with high precision to be perpendicular to the rotation axis with the help of a frequency-stabilized helium-neon laser in a Mach-Zehnder interferometer[46]. The residual target fluctuations in the normal direction are maintained $< z_R/5$ peak-to-valley, where $z_R \approx 10$ m is the Rayleigh range of the driving laser. Angular fluctuations are reduced to < 80 μrad peak-to-valley, limited by mechanical stress in the target's rotary bearing.

A high-speed mechanical beam shutter (*Uniblitz CS45*, 45 mm diameter, 14 ms opening time) in front of the OAP controls the shot sequence sent on target, and is protected during longer $\gtrsim$ 1-s durations between acquisitions from overheating due to the laser's average power by a preceding ceramic disk mounted on a slower flip mount. The target controller, made from an Arduino micro-controller board, *(i)* tracks the angular and radial positions of the laser-target interaction point and which of these positions have already been shot at, *(ii)* sets the target rotation speed according to the desired shot spacing (typically 100 μm), and *(iii)* triggers the shot sequence as well as the diagnostics detailed in section III E. For acquisition, the target controller triggers the slow shutter opening and sets the target rotation speed. Once an angular position with a fresh target surface has been reached, the fast shutter is triggered to open, and 14 ms later the diagnostics are triggered. After the desired acquisition time (typically 100 ms, thus averaging over 100 consecutive laser shots), the fast shutter closes, the target rotation slows down and the slow shutter closes. Once a full circle of shots at a given radius is completed, the target is translated laterally by typically 100 μm to commence a new circular shot pattern.

We exclusively use SiO_2 as target material in the form of uncoated 5 inch diameter substrates, polished to $\lambda/10$ flatness on both faces. With a 100 μm shot spacing, these targets can in principle take 1.2 million consecutive shots per face, corresponding to 20 min of continuous operation at 1 kHz. In practice, we take ≈ 1000 acquisitions of ≈ 100 shots per day of experiment, so that one target lasts approximately one month.

C. Plasma density gradient control

A spatially overlapped, time-delayed Pre-pulse is created by picking off $\approx 4\%$ of the Main pulse through a holey mirror, decreasing its size by a factor ≈ 2 in a Galilean telescope, and sending it through a delay stage. It is collinearly recombined with the Main pulse through a second holey mirror (M1 in figure 1) before being focused to a 13 μm FWHM spot with the same OAP. Its much larger size compared to the Main pulse leads to a spatially homogeneous plasma expansion on the target surface. The plasma density gradient scale length, $L_g \approx L_0 + c_s\tau$, is scanned by varying the lead time τ of the Pre-pulse before the Main pulse. Here, L_0 is the scale length increase due to the finite temporal contrast of the Main pulse. The plasma ex-

pansion velocity c_s is measured with the spatial domain interferometer (SDI) technique[19], detailed in section IV A.

The overlapped Pre-pulse (in grey-scale) and Main pulse (in color-scale) beam profiles in-focus are shown in figure 1(f). Whether at a fixed lead time or during a τ-scan, the spatial overlap of these two focal spots is extremely stable thanks to the laser's excellent pointing stability and to the use of a retro-reflector and a low-wobble motorized translation stage in the Pre-pulse delay line. The retro-reflector produces an elliptical polarization state of the Pre-pulse, which is remediated by a half-wave plate that rotates the major axis of the ellipse into the p-polarization direction.

D. Plasma density gradient calibration

The time-delayed Pre-pulse creates an initially quasi-step-like preplasma density profile, with an electron density n_0 in the half-space $x < 0$, the x-direction being perpendicular to the target surface. The free expansion of such a plasma can be described by a 1D isothermal (i.e. constant electron temperature T_e) model[47] yielding a time-dependent exponential electron density profile that starts dropping at $x = -c_s t$ from n_0 towards vacuum, given as,

$$n(x,t) = n_0 \exp\left[-\frac{x}{c_s t} - 1\right], \qquad (1)$$

Here, the gradient scale length $L_g = c_s t$ linearly increases with the so-called ion sound velocity $c_s = \sqrt{Z k_B T_e / m_i}$, where Z is the ion charge state, k_B the Boltzmann constant, and m_i the ion mass. This implies that, as long as the target surface's absorption coefficient for the Pre-pulse energy is intensity-independent, such that the resulting local electron temperature T_e is proportional to the local Pre-pulse fluence F, the local expansion velocity c_s at every position is proportional to $\sqrt{F}$.

As a daily routine measurement, this characteristic velocity c_s of the plasma expansion initiated by the Pre-pulse is determined with the SDI technique introduced by Bocoum *et al.*[19]. The principle of SDI is to interfere light reflected off the expanded plasma with light reflected off an unperturbed part of the target surface. The light is considered to reflect on the critical-density surface at depth x_c, where the electron density is $n_c \cos^2\theta_i$, with $n_c = \omega_0^2 m_e \varepsilon_0 / e^2$, the laser carrier angular frequency ω_0, the electron mass m_e, the vacuum permittivity ε_0 and the electron charge e. The phase shift due to the reflection at $x = x_c$ rather than at the initial target-vacuum boundary at $x = 0$ is given by (as in Bragg reflection)

$$\phi = 2\frac{\omega_0}{c} x_c \cos\theta_i. \qquad (2)$$

Dephasing due to propagation through the low-density tail of the plasma is at least an order of magnitude smaller and is thus neglected. The measured phase shift as a function of the Pre-pulse lead time τ thus tracks the position $x_c(\tau)$ of the critical density surface. Imposing the exponential shape of equation 1 (where time t is equivalent to τ) for the plasma density profile, this corresponds to the gradient scale length

$$L_g(\tau) = \frac{x_c(\tau)}{\ln\left[n_0/(n_c \cos^2\theta_i)\right] - 1}. \qquad (3)$$

Experimentally, SDI is implemented by inserting a periodic transmission mask of period a (in our case a hexagonal pattern of 3 mm holes with

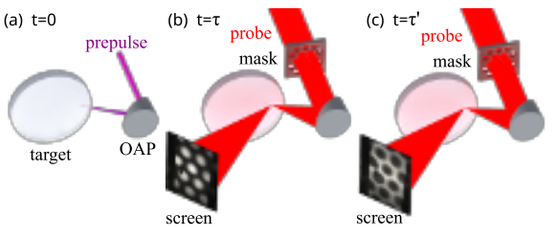

FIG. 2. Schematic representation of the experimental SDI measurement. (a) The Pre-pulse initiates the plasma expansion. (b) The probe beam, obtained by shaping the Main pulse with a mask into a hexagonal pattern of smaller beams, is delayed and focused onto the expanding plasma and gets reflected. At certain Pre-pulse lead times τ, the reflected near-field beam profile recreates the pattern imposed by the mask. (c) At certain Pre-pulse lead times, τ', this pattern is inverted, indicating a phase shift of π imposed on the reflected probe beam by the expanding plasma. The images displayed on the "screen" are actual recorded data from a typical SDI measurement.

a period $a = 4\,\mathrm{mm}$) into the near-field of the main beam, as shown in figure 2, thus transforming it into the probe beam for SDI. Upon focusing by the OAP, this turns into its far-field diffraction pattern on the target surface. In the paraxial approximation, this is given by the probe beam's spatial Fourier-transform, which is again a hexagonal pattern of "probe spots" (each of the same $\approx 1.8\ \mu$m-FWHM size as the main beam focus) with a period $d = \lambda_0 f/a$, where λ_0 is the light wavelength. For $\lambda_0 = 800\,\mathrm{nm}$ we thus obtain $d = 10\,\mu\mathrm{m}$. This means that the central (zeroth diffraction order) probe spot overlaps with the center of the Pre-pulse and thus with the nearly homogeneously expanding plasma with which the Main pulse would interact, while the surrounding hexagon of (first diffraction-order) probe spots overlaps with the wings of the 13-μm Pre-pulse spot, where the Pre-pulse fluence F_1 has dropped to $\approx 10\%$ of its peak value F_0.

The expanding plasma thus induces a phase shift $\Delta\phi = \phi_0 - \phi_1$ between the central (zeroth order) and the surrounding hexagon of (first order) probe spots. In the simplest case, the first order spots probe an unaffected target surface, so that $\phi_1 = 0$. In our case however, the first-order spots reflect off an expanding plasma "launched" by a finite local Pre-pulse fluence of $F_1 \approx 0.1F_0$, with the fluence F_0 at the Pre-pulse center. Two assumptions are now required: *(i)* Relying on the 1D isothermal expansion model mentioned above, we can write how much smaller the local expansion velocity at the location of the first order probe spots, c_s^1, will be compared to its value, c_s, at the center: $c_\mathrm{s}^1 = \sqrt{F_1/F_0}c_\mathrm{s}$. *(ii)* We set the maximum plasma density n_0 to be the same everywhere. By combining equations (2) and (3), we deduce that the gradient scale length at the Pre-pulse center, L_g, is proportional to the measurable phase shift $\Delta\phi$:

$$L_\mathrm{g}(\tau) = \alpha\,\Delta\phi(\tau),$$
$$\text{with}\,\alpha = \frac{\lambda_0/(4\pi\cos\theta_i)}{\{\ln[n_0/(n_\mathrm{c}\cos^2\theta_i)] - 1\}\left(1 - \sqrt{F_1/F_0}\right)}. \quad (4)$$

The measurement of $\Delta\phi$ is made by observing, through an interferometric band-pass filter around $\lambda_0 = 800\,\mathrm{nm}$, the modification of the probe beam's near-field profile (cf. Fig.1(a)). As demonstrated in ref.[19] and illustrated in figure 2, the pattern reverses every time the phase shift $\Delta\phi$ reaches an integer multiple of π. The pattern reversal is easily extracted from the recorded near-field images by tracing the "SDI contrast" defined as $C = [S_\mathrm{b}(\tau) - S_\mathrm{d}(\tau)]/[S_\mathrm{b}(\tau) + S_\mathrm{d}(\tau)]$, where S_b and S_d are the integrated signals over selected image areas that are initially (at $\tau = 0$) bright and dark, respectively. As visible in the examples shown in the left column of figure 3, the SDI contrast oscillates and its extrema mark the times, τ, when the dephasing, $\Delta\phi$, has increased by π. The resulting dephasing curve, $\Delta\phi(\tau)$, is found to be linear (at least for the first $\approx 20\,\mathrm{ps}$ or so), which through equation 4 corresponds to a linearly increasing $L_\mathrm{g} = c_\mathrm{s}\tau$, as expected from the 1D isothermal expansion model. Its slope is easily found by a fit on the linear range of data points and yields the sought-after expansion velocity, c_s, that is then used to calibrate the gradient scale length in experiments.

E. Diagnostics

The experimental set-up has been designed to simultaneously detect three observables resulting from the laser-PM interaction, namely the emission of HHG radiation, energetic electrons, and proton beams. This is achieved with three dedicated diagnostics, illustrated in figure. 1(b),(c),(d) and (e) detailed below. These are complemented by a fourth one consisting of recording the reflected laser beam's near-field beam profile on a screen with a CCD camera (12-bit, *Pixelink PL-B957U*), as illustrated in figure 1(a).

1. XUV spectrometer

A rectangular hole in the screen for the near-field beam profile transmits light within the angular acceptance of the XUV spectrometer that spectrally characterizes the HHG emission. The spectrometer consists of an aberration-corrected, flat-field concave grating (*Hitachi 001-0639*, 600 groves/mm, incidence angle $\alpha = 85.3°$, optimized for wavelenegths $\lambda \approx 22 - 124\,\mathrm{nm}$) that images in the hori-

zontal dimension the $\sim 1\ \mu m$ size HHG source spot on the PM surface, and spectrally disperses it onto an image plane. Beam propagation is hardly influenced in the vertical dimension which thus provides angular resolution to the resulting spectrograph. A single-stack micro-channel plate (MCP) coupled with a P46 phosphor screen (*Photonis Scientific, APD 1 PS 97X79/32/25/8 I 40:1 P46*) is placed in the image plane. It is finally imaged using a CCD camera (12-bit *PCO Pixelfly VGA*). Figure 1(a) shows a typically recorded XUV spectrograph. The MCP is time-gated for 200 ns synchronously with the laser pulses to suppress background signal from longer incoherent plasma emission. The P46 phosphor screen has a decay time of ≈ 300 ns enabling detection at kHz repetition rate.

2. Electron diagnostics

The angular electron distribution is measured with a scintillating screen[48] (*Carestream Lanex fast*), placed ≈ 20 cm from the point of interaction, covering a small but sufficient angular range between the target normal and the specular direction, for $30^\circ < \phi < 50^\circ$, where ϕ is the angle w.r.t the target normal in the plane of incidence. The front side of the Lanex-screen is covered with a 15 μm thick aluminium foil to block visible light and low-energy electrons ($E_k < 150$ keV). Detection of low-energy electrons is also suppressed by the substrate of the Lanex-screen. The green light emission of the Lanex-screen is imaged by a CCD camera (12-bit, *Pixelink PL-B957U*) through an interferometric band-pass filter. The decay time of such a Lanex screen[49] is typically < 1 ms and hence, these screens are compatible for operation at a kHz repetition rate.

The electron energy spectrum can be measured by inserting a purpose-built electron spectrometer in front of the same Lanex screen with motorized linear stages. It comprises of a 0.5-mm pinhole in a Pb-disk, followed by a separately insertable pair of neodymium magnets ($B_0 \approx 80$ mT over ≈ 20 mm). The magnetic field map has been measured with a Hall probe and injected into a numerical electron trajectory calculation to calibrate the electron energy vs. the position along the trace of deflected electrons on the Lanex-screen. The pinhole, located at ≈ 8 cm from the point of interaction, samples the beam at an angle ϕ selected by the insertion position with an angular acceptance of $\approx 0.4^\circ$. In order not to block the HHG beam, ϕ is limited to values $< 40^\circ$, which is often still slightly off the electron beam center (cp. Fig. 1c). An acquisition with the inserted pinhole but without the magnets calibrates the zero-position of the undeflected electron beam with respect to which the deflection distance is measured once the magnets are inserted.

3. Proton diagnostics

Accelerated protons along the target normal are spectrally characterized using an in-house built Thomson parabola spectrometer (TPS). A 300 μm pin-hole placed at about 60 cm from the point of interaction selects protons emitted along the target normal direction, which are then dispersed in energy and charge-mass ratio by a 2 kV/cm electric and an anti-parallel 300 mT magnetic field, created by 50 mm long electrodes and 15 mm long magnets, respectively. Figure 1(d) shows a typical recorded TPS trace. Protons can be easily and uniquely distinguished from the heavier ions due to their smallest mass-to-charge ratio. The TPS trace is recorded with an MCP-Phosphor screen assembly imaged by a CCD camera (12-bit, *Pixelink PL-B957U*). The proton energy range for this TPS setup has a lower bound at ≈ 75 keV given by the MCP aperture, and an upper bound of ≈ 1 MeV, given by the spatial width of the proton trace on the MCP and a corresponding relative energy error that surpasses 10% at 1 MeV.

Alternatively, angularly resolved proton spectra can be measured with a movable time-of-flight (TOF) detector. It consists of a 6 mm diameter MCP, placed ≈ 37.5 cm from the point of interaction, and mounted on a linear translation stage moving parallel to the target surface. This TOF-MCP has an angular acceptance of 0.9°, small enough to neglect the convolution owing to the finite size of the detector. The transient MCP current is read out using a *KEYSIGHT MSOS804A* 8 GHz oscilloscope capable of individually recording all ~ 100 shots in one acquisition when operated in segmented memory acquisition mode. Figure 1(e) shows a typically

recorded TOF trace. This measurement was taken for a pulse duration of 27 fs, no prepulse ($\tau = 0\,ps$) and at the target normal direction ($\phi = 0°$). The blue line shows an average of 100 consecutive shots, smoothed by a rolling average over the response time of the detector of 1 ns. The shaded gray area shows the standard deviation of the shots. The first sharp peak corresponds to the electromagnetic radiation emitted from the laser-plasma interaction and defines the time $t = 0$. The first protons start to arrive at $t \approx 50$ ns, with a peak signal at $t \approx 90$ ns, followed by the heavier ions with a signal peaked at $t \approx 180$ ns. The onset of overlap with the carbon ions' TOF signal gives the lower bound at ≈ 50 keV of the proton energy range for the TOF detector. The noise at ≤ 51 ns is due to electrical noise in the circuit, and degrades the signal-to-noise ratio such that at energies $\gtrsim 0.3$ MeV, the spectrum is more reliably measured with the TPS.

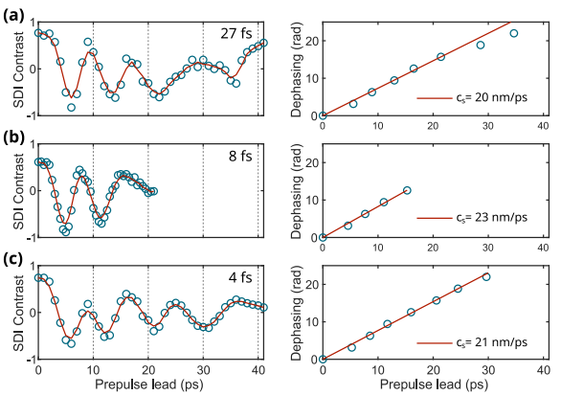

FIG. 3. Experimental SDI contrast curves (left, circles are raw data, lines are smoothed data) and extracted dephasing curves curve $\Delta\phi(\tau)$ (right, circles are extracted data, lines are linear fits including points with $\tau < 20$ ps) for SDI scans obtained for driving laser pulse durations of 27 fs (a), 8 fs (b) and 4 fs (c).

IV. EXPERIMENTAL RESULTS

A. Plasma density gradient measurement

The plasma density profile on the target surface is a critical experimental parameter, be it for HHG[13,16–18,50], electron acceleration[7,13,16,22], or proton acceleration[20]. As a daily routine measurement, the characteristic plasma expansion velocity c_s initiated by the time delayed Pre-pulse is determined with the SDI technique introduced by Bocoum *et al.*[19] and as described in section III D.

Figure 3 shows a series of SDI measurements that answers the question whether the plasma expansion initiated by the Pre-pulse varies with laser pulse duration. Since neither the energy nor the spatial profile of the Pre-pulse vary with pulse duration, its *fluence* remains the same (≈ 50 J/cm^2) and only its *intensity* varies. The question thus comes down to whether the Pre-pulse absorption coefficient is intensity-dependent, which would lead to varying T_e and thus varying c_s. The telescope and wave plate traversed by the Pre-pulse add a group delay and a third-order dispersion of ≈ 260 fs^2 and ≈ 200 fs^3, respectively. As a consequence, the 27 fs pulse is stretched to 38 fs with a peak intensity of 1.1×10^{15} W/cm^2, the 8 fs pulse is stretched to ≈ 100 fs with a peak intensity of 0.5×10^{15} W/cm^2, and the 4 fs pulse is stretched to ≈ 200 fs, with a profile dominated by a ≈ 40 fs spike with a peak intensity of 0.7×10^{15} W/cm^2. As visible in figure 3, the three cases lead to very similar expansion velocities, with a variation clearly below the uncertainty of the SDI method itself. We conclude that the c_s-value is independent of the Pre-pulse duration in the range covered by our experiments. This intensity independence corroborates the proportionality $c_s \propto \sqrt{F}$, which is one of the strong assumptions used in the SDI-analysis, detailed in section III D.

The slope of the $\Delta\phi(\tau)$-curves decreases for longer delays, $\tau > 20$ ps, indicating a decreasing velocity, c_s, and thus a cooling of the plasma electrons through transfer of energy to the ions. The L_g-values relevant to (most of) our PM experiments are however reached before these effects set in, such that the linear evolution, $L_g = c_s\tau + L_0$, remains valid.

We estimate the small offset $L_0 < \lambda_0/50$, since we clearly observe CWE harmonics (see discussion below), which are not generated efficiently with longer gradients[6,21].

B. Short and intermediate plasma density gradients

All data reported here are acquired and integrated over 100 ms long bursts of laser pulses at 1 kHz repetition rate, unless stated otherwise.

Figure 4 shows the simultaneously measured HHG, electron and proton spectra for a range of short to intermediate plasma density gradients, with relativistically intense main driving pulses of (a) 29 fs ($a_0 = 1.0$ for $\lambda_0 = 800$ nm) and (b) 4 fs ($a_0 = 2.1$ for $\lambda_0 = 780$ nm) duration. The gradient scale length is calculated, up to the small offset L_0, as $L_g - L_0 = c_s\tau$ (top axis) from the plasma expansion velocity $c_s = 18$ nm/ps, measured as described in section IV A, and the Pre-pulse lead time τ (bottom axis). Each of the scans in figure 4 have been individually normalized to its maximum value and hence the spectral intensity cannot be directly compared. The HHG spectrum (figure 4 top frame) is angularly integrated over the full detected range of $[-35\text{ mrad}, +35\text{ mrad}]$. The spectral response of the MCP has not been taken into account so as to enhance the visibility of higher harmonic orders.

We can identify the two regimes for HHG: CWE-HHG at steep gradients ($L_g - L_0 < 0.03\lambda_0$) and RHHG at more gentle gradients of $L_g - L_0 \approx 0.03\lambda_0 - 0.2\lambda_0$[13,16]. In the CWE regime, the intensity-dependence of the Brunel electron trajectories leads to a temporal aperiodicity of the emitted attosecond pulse train and, hence, to broadened harmonics in the spectral domain[13,21]. In contrast, the RHHG emission in the moderately relativistic regime ($a_0 \sim 1$) is Fourier-limited[34], corresponding to narrower spectral widths of the harmonics as compared to the CWE-HHG, as observed in figure 4(a) (top frame) with 29 fs driving pulse duration. However, this transition between the CWE and RHHG regimes becomes less distinct with shorter driving pulse durations ($a_0 > 1$) since the harmonics emerge in the spectrograph from the interference between fewer attosecond pulses. In figure 4(b), for a 4 fs driving pulse, around an optimal $L_g - L_0 \approx 0.08\lambda_0$, the HHG spectrum extends well beyond the CWE cutoff of 30 eV for an SiO_2 target, which is definitive proof of RHHG.

The electron energy spectrum (figure 4, middle frame) is simultaneously measured at $\phi = 38^\circ$ or $\phi = 40^\circ$. These positions do not sample the center of the electron beam, which is located a few degrees closer towards the specular direction (see Fig. 1(c)), but they allow simultaneous detection of the HHG emission. At the steepest gradients, where the CWE-HHG is optimum, low electron energy and charge is measured for both driving pulse durations of 29 fs and 4 fs. Such anti-correlated electron beam charge and CWE-HHG has been previously observed at sub-relativistic intensities with 30 fs driving laser pulses[15]. Here, we reproduce the anti-correlation with relativistic intensities $a_0 > 1$, and measure not only the electron charge but also electron energies. Correlated with RHHG, we measure maximum electron charge and energies up to 1.5 MeV. Higher energies are expected in the center of the electron beam. The apparent dip in the electron spectra around $L_g - L_0 \sim 0.17\lambda$ is suspected to be linked to a moving electron beam with a spatially inhomogeneous spectrum[13].

The electron beam spatial profile and pointing can be measured by removing the spectrometer-setup in front of the lanex-screen with a motorized stage. Such measurements have been the focus of earlier publications[7,14–16,22].

Figure 4 (bottom frame) shows the proton energy spectrum simultaneously measured with the TPS along the target normal direction ($\phi = 0^\circ$). We observe that for both driving pulse durations, the proton energies benefit from the steepest plasma density gradients and are correlated with CWE-HHG. This suggests Brunel electrons to play an important role in the acceleration mechanism[8,20]. If an optimal plasma gradient exists for efficient acceleration of protons, it is below our resolution limit of $L_0 \approx 0.01\lambda_0$. The highest proton energies of 0.25 MeV are obtained with 29 fs driving pulses for the steepest density gradients and drop below the detection threshold of 0.1 MeV for $L_g > 0.1\lambda_0$. The cut-off energy decreases to ≈ 0.15 MeV for shorter 4 fs driving pulses.

Figure 5(a,b) shows the HHG spectra and proton energy spectra measured with the TPS for the steepest plasma density gradient and longer driving pulses obtained by adding positive group delay dispersion (GDD). In the HHG spectra (Fig.5(a)), we observe the typical behavior of CWE harmonics: the temporal chirp resulting from the posi-

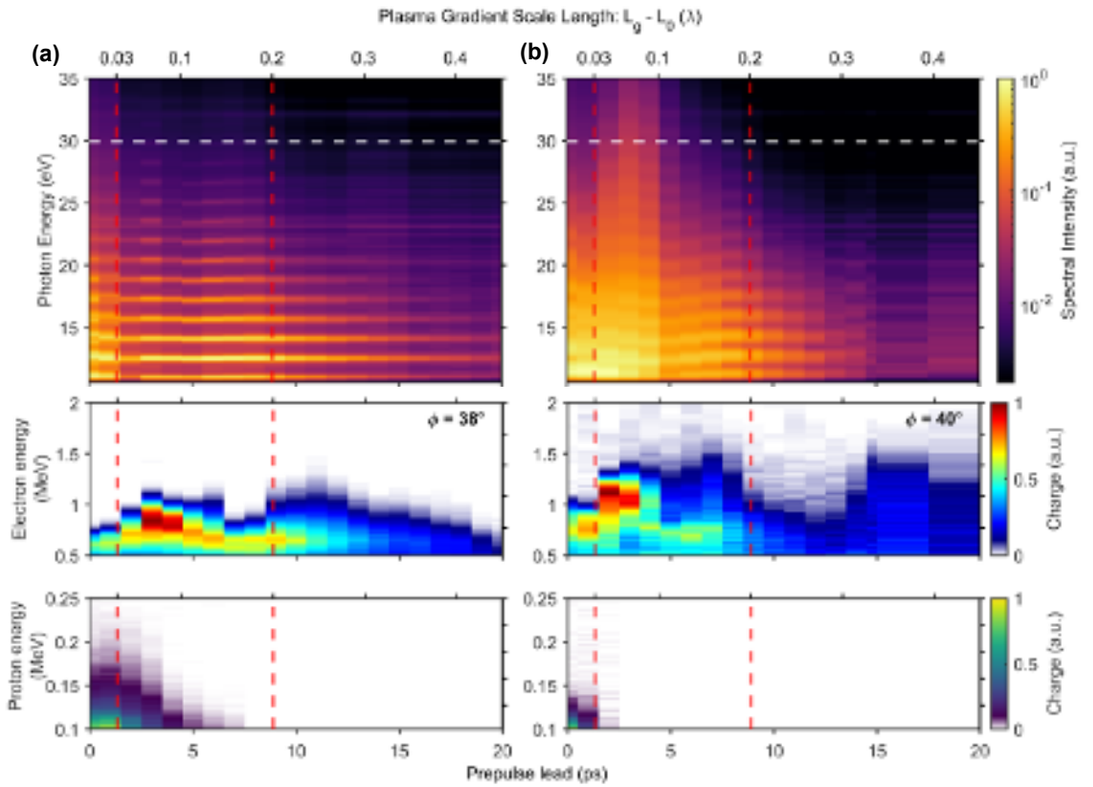

FIG. 4. Simultaneously measured angularly integrated HHG spectrum (top), electron spectrum measured for $\phi = 38°$ or $\phi = 40°$ (middle), and proton spectrum at $\phi = 0°$(bottom) as a function of the plasma density gradient scale length, for different driving pulse durations (a) 29 fs ($a_0 = 1.0$), and (b) 4 fs ($a_0 = 2.1$). The dashed white line marks the photon cut-off energy for CWE-HHG. The dashed red lines mark $L_g - L_0 \sim 0.03\lambda$ and $L_g - L_0 \sim 0.2\lambda$.

tive GDD compensates the temporal aperiodicity of the emitted attosecond pulse train which leads to a narrowing of the harmonic spectral width[21]. The near-constant conversion efficiency of the CWE process[6] over a wide intensity range lets the HHG signal persist despite the laser intensity being reduced by an order of magnitude for the stretched pulses, before it vanishes at 850-fs pulse duration and only background plasma emission is detected. These observations firmly establish that it is CWE-HHG that is correlated with the proton acceleration. In the proton spectra (Fig.5(b)), we observe an optimum between 100 fs and 300 fs, yielding ≈ 0.45 MeV protons. In this acceleration regime, which we have described as radiation pressure assisted Coulomb explosion (RPACE)[20], protons are accelerated only during the the interaction time of the pulse. They therefore benefit from a longer driving pulse duration despite the corresponding drop in laser intensity[8,20]. Figures 5(c,d) show the angle-resolved proton energy spectrum measured with the moving TOF detector, averaging over 100 acquisitions of successive single shots at 1 kHz repetition rate, for two different driving pulse durations, compressed 29 fs (c) and chirped 200 fs (d), at the steepest plasma gradient. In both cases, we observe a very low $\leq 4°$ FWHM divergence of the proton beam. This is significantly lower than the 16° FWHM reported earlier[42], which may be the result of a higher temporal contrast ratio of the driving

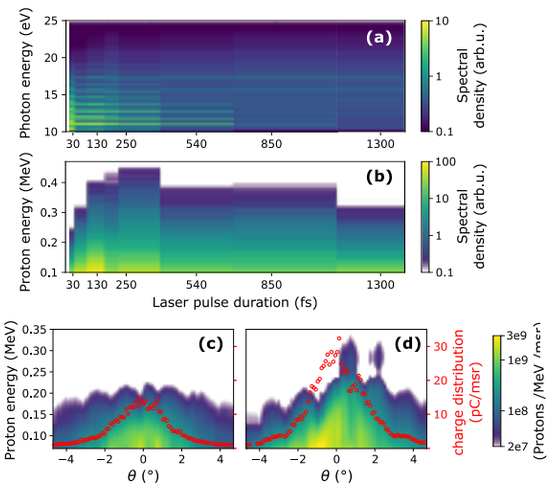

FIG. 5. Simultaneously acquired CWE-HHG spectra (a) and proton energy spectra measured with TPS (b) at the steepest density gradients for different driving pulse durations obtained by adding GDD to 29-fs laser pulses. Angular proton energy spectrum obtained for (c) 29 fs and (d) 200 fs driving pulses measured by the moving TOF detector. Red circles show the spectrally integrated angular charge distribution of the proton beam. $\phi = 0°$ is the target normal direction.

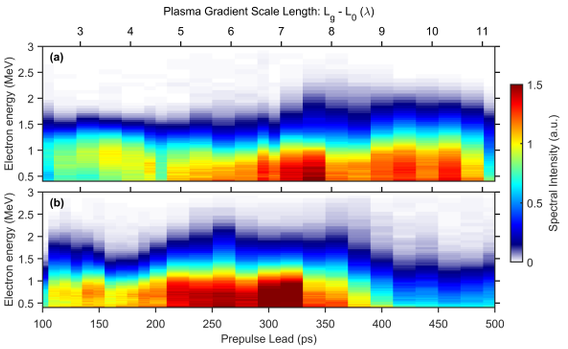

FIG. 6. Electron spectrum measured at $\phi = 40°$ for (a) 7 fs and (b) 4 fs driving laser pulse duration and varying plasma density scale length.

laser in our case.

C. Long density gradients regime

All data reported here are acquired and integrated over 100 ms long bursts of laser pulses at 1 kHz repetition rate.

For long density gradients ($L_g \geq \lambda_0$), RHHG disappears due to the onset of chaotic electron dynamics in the near-critical-density layer of the plasma density gradient[13]. However, before reaching that layer, the laser propagates through the sub-critical tail of the plasma density profile. In the zone of density $\sim n_c/10$, few-cycle laser pulses < 10 fs are able to resonantly excite a strong plasma wakefield. Electrons can be injected into this laser wakefield by ionization and then get accelerated to relativistic energies. The plasma wavefront is rotated by the density gradient and electrons are pushed away from the specular direction[22]. Figure 6 shows the electron spectra measured in this regime for gradient scale lengths up to $\approx 10\lambda_0$, reaching up to 2.6 MeV. Note that the gradient scale lengths given by the top axis result from the same 18 nm/ps expansion velocity, as determined for the initial expansion phase with Pre-pulse lead times < 20 ps. As discussed in connection with figure 3, we know that the expansion slows down considerably at longer times, so that the true gradient scale lengths are certainly shorter than those indicated in Figure 6.

During this scan over long $L_g \geq \lambda_0$, the simultaneously running HHG and proton diagnostics recorded only background noise signals, which are thus not shown. This anti-correlation with the relativistic electron beam corroborates its origin from the underdense part of the surface plasma and its generation before the (chaotic[13]) reflection of the laser in the critical-density-region.

V. SUMMARY

We have reported the first simultaneous measurements of HHG, electron beams and proton beams from a laser-driven PM. The kHz laser repetition rate allowed exploring a wide range of laser and plasma parameters. We have presented spectral measurements of HHG, electrons and protons as a function of controlled plasma density scale

lengths ranging from $0.01\lambda_0 - 0.2\lambda_0$ for three different driving pulse durations: 29 fs ($a_0 = 1.0$), 7 fs ($a_0 = 2.0$), and 4 fs ($a_0 = 2.1$). Such simultaneous measurements vastly expand the level of characterization of relativistic PMs. While ensuring identical interaction conditions on target, we observe direct correlations between the CWE-HHG and Brunel-dominated accelerated proton beams, and the anti-correlated emission of relativistic electron beams. We also observe direct correlation between the RHHG and the emitted electron beams. At extremely long density gradients, only with few-optical-cycle driving laser pulses, we measure up to 2.5 MeV electrons accelerated by the laser wakefield formed in the gradient.

We also measured proton spectra for a wide range of driving pulse durations, from 4 fs up to 1.5 ps, at the steepest plasma density gradient, and find an optimum pulse duration range for proton yield, between 100 fs and 400 fs, under such conditions. These novel measurements of low-divergence ($< 4^\circ$ FWHM) font-side-accelerated proton beams with a controlled density gradient hold intrinsic value of their own. The exceptional beam properties, along with the possibility of scaling with the driving laser energy to multi-MeV proton energy levels[20], are promising for applications in the field of medicine, for example to produce radioisotopes[44].

To conclude, this work is a decisive step towards a highly detailed characterization of fundamental PM dynamics and the optimal generation of energetic particle and radiation beams exploiting the high repetition rate of our laser system.

Additionally, we have also implemented carrier-envelope phase control, with feedback at the full repetition rate of the laser system. This should enable the generation of isolated intense attosecond pulses[51] with high conversion efficiencies[52], by controlling the collective plasma dynamics at a the sub-light-cycle level.

ACKNOWLEDGMENTS

This work has been supported by the Agence Nationale pour la Recherche (ANR-14-CE32-0011-03 APERO), the European Union's Horizon 2020 research and Innovation program (Advanced Grant ExCoMet 694596), and LASERLAB-Europe (grant agreements 654148 and 871124).

STATEMENT OF DATA AVAILABILITY

The data that supports the findings of this study are available from the corresponding author upon reasonable request.

AUTHOR DECLARATIONS

The authors have no conflicts of interests to disclose.

[1]Henry C. Kapteyn, Margaret M. Murnane, Abraham Szoke, and Roger W. Falcone. Prepulse energy suppression for high-energy ultrashort pulses using self-induced plasma shuttering. *Opt. Lett.*, 16(7):490–492, Apr 1991.

[2]G. Doumy, F. Quéré, O. Gobert, M. Perdrix, Ph. Martin, P. Audebert, J.C. Gauthier, J.-P. Geindre, and T. Wittmann. Complete characterization of a plasma mirror for the production of high-contrast ultraintense laser pulses. *Physical Review E*, 69:026402, Feb 2004.

[3]B. Dromey, S. Kar, M. Zepf, and P. Foster. The plasma mirror—a subpicosecond optical switch for ultrahigh power lasers. *Review of Scientific Instruments*, 75:645, Feb 2004.

[4]M. P. Kalashnikov, E. Risse, H. Schönnagel, and W. Sandner. Double chirped-pulse-amplification laser: a way to clean pulses temporally. *Optics Letters*, 30(8):923–925, Apr 2005.

[5]Sudipta Mondal, Qiliang Wei, Muhammad Ashiq Fareed, Hassan A. Hafez, Xavier Ropagnol, Shuhui Sun, Subhendu Kahaly, and Tsuneyuki Ozaki. Ultrafast Plasma Electron Dynamics: A Route to Terahertz Pulse Shaping. *Phys. Rev. Applied*, 13(3):034044, 2020.

[6]C. Thaury and F. Quéré. High-order harmonic and attosecond pulse generation on plasma mirrors: basic mechanisms. *Journal of Physics B: Atomic, Molecular and Optical Physics*, 43(21):213001, 2010.

[7]M. Thévenet, A Leblanc, S. Kahaly, H. Vincenti, A. Vernier, F. Quéré, and J. Faure. Vacuum laser acceleration of relativistic electrons using plasma mirror injectors. *Nature Physics*, 12:355—-360, 2016.

[8]M. Veltcheva, A. Borot, C. Thaury, A. Malvache, E. Lefebvre, A. Flacco, R. Lopez-Martens, and V. Malka. Brunel-Dominated Proton Acceleration with a Few-Cycle Laser Pulse. *Physical Review Letters*, 108(7):075004, 2012.

[9]J. Rothhardt, G.. K Tadesse, W. Eschen, and J. Limpert. Table-top nanoscale coherent imaging with xuv light. *Journal of Optics*, 20(11):113001, oct 2018.

[10]X. Ribeyre, R. Capdessus, J. Wheeler, E. d'Humières, and G. Mourou. Multiscale study of high energy attosecond pulse

interaction with matter and application to proton–boron fusion. *Scientific Reports*, 12(1):4665, Mar 2022.

[11] J. Doyen, A. T. Falk, V. Floquet, J. Hérault, and J.-M. Hannoun-Lévi. Proton beams in cancer treatments: Clinical outcomes and dosimetric comparisons with photon therapy. *Cancer Treatment Reviews*, 43:104–112, 2016.

[12] A. Döpp, C. Eberle, S. Howard, F. Irshad, J. Lin, and M. Streeter. Data-driven science and machine learning methods in laser-plasma physics. *arXiv*, arXiv:2212.00026, 2023.

[13] L. Chopineau, A. Leblanc, G. Blaclard, A. Denoeud, M. Thévenet, J-L. Vay, G. Bonnaud, Ph. Martin, H. Vincenti, and F. Quéré. Identification of Coupling Mechanisms between Ultraintense Laser Light and Dense Plasmas. *Physical Review X*, 9(1):011050, 2019.

[14] L. Chopineau, G. Blaclard, A. Denoeud, H. Vincenti, F. Quéré, and S. Haessler. Sub-laser-cycle control of relativistic plasma mirrors. *Physical Review Research*, 4(1):L012030, 2022.

[15] M. Bocoum, M. Thévenet, F. Böhle, B. Beaurepaire, A. Vernier, A. Jullien, J. Faure, and R. Lopez-Martens. Anticorrelated emission of high harmonics and fast electron beams from plasma mirrors. *Physical Review Letters*, 116:185001, 2016.

[16] S. Haessler, M. Ouillé, J. Kaur, M. Bocoum, F. Böhle, D. Levy, L. Daniault, A. Vernier, J. Faure, and R. Lopez-Martens. High-harmonic generation and correlated electron emission from relativistic plasma mirrors at 1 kHz repetition rate. *Ultrafast Science*, 2022:9893418, 2022.

[17] M. Zepf, G. D. Tsakiris, G. Pretzler, I. Watts, D. M. Chambers, P. A. Norreys, U. Andiel, A. E. Dangor, K. Eidmann, C. Gahn, A. Machacek, J. S. Wark, and K. Witte. Role of the plasma scale length in the harmonic generation from solid targets. *Physical Review E*, 58:R5253, 1998.

[18] S. Kahaly, S. Monchocé, H. Vincenti, T. Dzelzainis, B. Dromey, M. Zepf, Ph. Martin, and F. Quéré. Direct observation of density-gradient effects in harmonic generation from plasma mirrors. *Physical Review Letters*, 110:175001, 2013.

[19] M. Bocoum, F. Böhle, A. Vernier, A. Jullien, J. Faure, and R. Lopez-Martens. Spatial-domain interferometer for measuring plasma mirror expansion. *Optics Letters*, 40(13):3009–3012, 2015.

[20] D. Levy, I. A. Andriyash, S. Haessler, J. Kaur, M. Ouillé, A. Flacco, E. Kroupp, V. Malka, and R. Lopez-Martens. Low divergence proton beams from a laser-plasma accelerator at kHz repetition rate. *Physical Review Accelerators and Beams*, 25(9):093402, 2022.

[21] F. Quéré, C. Thaury, P. Monot, S. Dobosz, Ph. Martin, J.-P. Geindre, and P. Audebert. Coherent wake emission of high-order harmonics from overdense plasmas. *Physical Review Letters*, 96:125004, 2006.

[22] N. Zaïm, F. Böhle, M. Bocoum, A. Vernier, S. Haessler, X. Davoine, L. Videau, J. Faure, and R. Lopez-Martens. Few-cycle laser wakefield acceleration on solid targets with controlled plasma scale length. *Physics of Plasmas*, 26(3):033112, 2019.

[23] B. Dromey, M. Zepf, A. Gopal, K. Lancaster, M. S. Wei, K. Krushelnick, M. Tatarakis, N. Vakakis, S. Moustaizis, R. Kodama, M. Tampo, C. Stoeckl, R. Clarke, H. Habara, D. Neely, S. Karsch, and P. Norreys. High harmonic generation in the relativistic limit. *Nature Physics*, 2:456–459, Jan 2006.

[24] Y. Nomura, R. Horlein, P. Tzallas, B. Dromey, S. Rykovanov, Zs Major, J. Osterhoff, S. Karsch, L. Veisz, M. Zepf, D. Charalambidis, F. Krausz, and G. D. Tsakiris. Attosecond phase locking of harmonics emitted from laser-produced plasmas. *Nature Physics*, 5:124–128, 2008.

[25] L. Chopineau, A. Denoeud, A. Leblanc, E. Porat, P. Martin, H. Vincenti, and F. Quéré. Spatio-temporal characterization of attosecond pulses from plasma mirrors. *Nature Physics*, 17:968–973, June 2021.

[26] R. Lichters, J. Meyer-ter-Vehn, and A. Pukhov. Short-pulse laser harmonics from oscillating plasma surfaces driven at relativistic intensity. *Physics of Plasmas*, 3(9):3425–3437, 1996.

[27] T. Baeva, S. Gordienko, and A. Pukhov. Theory of high-order harmonic generation in relativistic laser interaction with overdense plasma. *Physical Review E*, 74:046404, 2006.

[28] F. Brunel. Not-so-resonant, resonant absorption. *Physical Review Letters*, 59:52–55, 1987.

[29] A. Gonoskov. Theory of relativistic radiation reflection from plasmas. *Physics of Plasmas*, 25(1):013108, 2018.

[30] D. an der Brügge and A. Pukhov. Enhanced relativistic harmonics by electron nanobunching. *Physics of Plasmas*, 17(3):033110, 2010.

[31] J. M. Mikhailova, M. V. Fedorov, N. Karpowicz, P. Gibbon, V. T. Platonenko, A. M. Zheltikov, and F. Krausz. Isolated Attosecond Pulses from Laser-Driven Synchrotron Radiation. *Physical Review Letters*, 109:245005, 2012.

[32] B. Dromey, S. Rykovanov, M. Yeung, R. Hörlein, D. Jung, D. C. Gautier, T. Dzelzainis, D. Kiefer, S. Palaniyppan, R. Shah, J. Schreiber, H. Ruhl, J. C. Fernandez, C. L. S. Lewis, M. Zepf, and B. M. Hegelich. Coherent synchrotron emission from electron nanobunches formed in relativistic laser–plasma interactions. *Nature Physics*, 8:804–808, 2012.

[33] M. R. Edwards and J. M Mikhailova. The x-ray emission effectiveness of plasma mirrors: Reexamining power-law scaling for relativistic high-order harmonic generation. *Scientific Reports*, 10:5154, 2020.

[34] F. Quéré, C. Thaury, J-P. Geindre, G. Bonnaud, P. Monot, and Ph. Martin. Phase properties of laser high-order harmonics generated on plasma mirrors. *Physical Review Letters*, 100:095004, Mar 2008.

[35] M. Yeung, B. Dromey, D. Adams, S. Cousens, R. Hörlein, Y. Nomura, G. D. Tsakiris, and M. Zepf. Beaming of High-Order Harmonics Generated from Laser-Plasma Interactions. *Physical Review Letters*, 110(16):165002, 2013.

[36] A. Leblanc, S. Monchocé, H. Vincenti, S. Kahaly, J.-L. Vay, and F. Quéré. Spatial Properties of High-Order Harmonic Beams from Plasma Mirrors: A Ptychographic Study. *Phys. Rev. Lett.*, 119(15):155001, 2017.

[37] M. Thévenet, H. Vincenti, and J. Faure. On the physics of electron ejection from laser-irradiated overdense plasmas. *Physics of Plasmas*, 23(6):063119, 2016.

[38] S. C. Wilks, A. B. Langdon, T. E. Cowan, M. Roth, M. Singh, S. Hatchett, M. H. Key, D. Pennington, A. MacKinnon, and R. A. Snavely. Energetic proton generation in ultra-intense laser–solid interactions. *Physics of Plasmas*, 8(2):542–549, 2001.

[39]R. A. Snavely, M. H. Key, S. P. Hatchett, T. E. Cowan, M. Roth, T. W. Phillips, M. A. Stoyer, E. A. Henry, T. C. Sangster, M. S. Singh, S. C. Wilks, A. MacKinnon, A. Offenberger, D. M. Pennington, K. Yasuike, A. B. Langdon, B. F. Lasinski, J. Johnson, M. D. Perry, and E. M. Campbell. Intense high-energy proton beams from petawatt-laser irradiation of solids. *Physical Review Letters*, 85:2945–2948, 2000.

[40]A. Macchi, M. Borghesi, and M. Passoni. Ion acceleration by superintense laser-plasma interaction. *Reviews of Modern Physics*, 85:751–793, 2013.

[41]S. Kar, K. Markey, P. T. Simpson, C. Bellei, J. S. Green, S. R. Nagel, S. Kneip, D. C. Carroll, B. Dromey, L. Willingale, E. L. Clark, P. McKenna, Z. Najmudin, K. Krushelnick, P. Norreys, R. J. Clarke, D. Neely, M. Borghesi, and M. Zepf. Dynamic control of laser-produced proton beams. *Physical Review Letters*, 100:105004, 2008.

[42]B. Hou, J. Nees, J. Easter, J. Davis, G. Petrov, A. Thomas, and K. Krushelnick. Mev proton beams generated by 3 mJ ultrafast laser pulses at 0.5 khz. *Applied Physics Letters*, 95(10):101503, 2009.

[43]L. Torrisi, A.M. Mezzasalma, S. Gammino, J. Badziak, P. Parys, J. Wolowski, L. Laska, and G. Franco. Ion implantation induced by cu ablation at high laser fluence. *Applied Surface Science*, 252(24):8533–8538, 2006.

[44]S. Fritzler, V. Malka, G. Grillon, J. P. Rousseau, F. Burgy, E. Lefebvre, E. d'Humières, P. McKenna, and K. W. D. Ledingham. Proton beams generated with high-intensity lasers: Applications to medical isotope production. *Applied Physics Letters*, 83(15):3039–3041, 2003.

[45]M. Ouillé, A. Vernier, F. Böhle, M. Bocoum, A. Jullien, M. Lozano, JP Rousseau, Z. Cheng, D. Gustas, A. Blumenstein, P. Simon, S. Haessler, J. Faure, T. Nagy, and R. Lopez-Martens. Relativistic-intensity near-single-cycle light waveforms at kHz repetition rate. *Light Science & Applications*, 9(1):2047–7538, 2020.

[46]A. Borot, D. Douillet, G. Iaquaniello, T. Lefrou, P. Audebert, J.-P. Geindre, and R. Lopez-Martens. High repetition rate plasma mirror device for attosecond science. *Review of Scientific Instruments*, 85(1):013104, 2014.

[47]P. Mora. Plasma expansion into a vacuum. *Physical Review Letters*, 90(18):185002, 2003.

[48]Y. Glinec, J. Faure, A. Guemnie-Tafo, V. Malka, H. Monard, J. P. Larbre, V. De Waele, J. L. Marignier, and M. Mostafavi. Absolute calibration for a broad range single shot electron spectrometer. *Review of Scientific Instruments*, 77(10):103301, 2006.

[49]R. Morlotti, M. Nikl, M. Piazza, and C. Boragno. Intrinsic conversion efficiency of X-rays to light in Gd2O2S : Tb3+ powder phosphors. *Journal of Luminescence*, 72-74:772–774, 1997.

[50]C. Rödel, an der Brügge, J. Bierbach, M. Yeung, T. Hahn, B. Dromey, S. Herzer, S. Fuchs, A. Galestian Pour, E. Eckner, M. Behmke, M. Cerchez, O. Jäckel, D. Hemmers, T. Toncian, M. C. Kaluza, A. Belyanin, G. Pretzler, O. Willi, A. Pukhov, M. Zepf, and G. G. Paulus. Harmonic generation from relativistic plasma surfaces in ultrasteep plasma density gradients. *Physical Review Letters*, 109:125002, 2012.

[51]F. Böhle, M. Thévenet, M. Bocoum, A. Vernier, S. Haessler, and R. Lopez-Martens. Generation of XUV spectral continua from relativistic plasma mirrors driven in the near-single-cycle limit. *Journal of Physics: Photonics*, 2(3):034010, 2020.

[52]O. Jahn, V. E. Leshchenko, P. Tzallas, A. Kessel, M. Krüger, A. Münzer, S. A. Trushin, G. D. Tsakiris, S. Kahaly, D. Kormin, L. Veisz, V. Pervak, F. Krausz, Z. Major, and S. Karsch. Towards intense isolated attosecond pulses from relativistic surface high harmonics. *Optica*, 6(3):280–287, 2019.

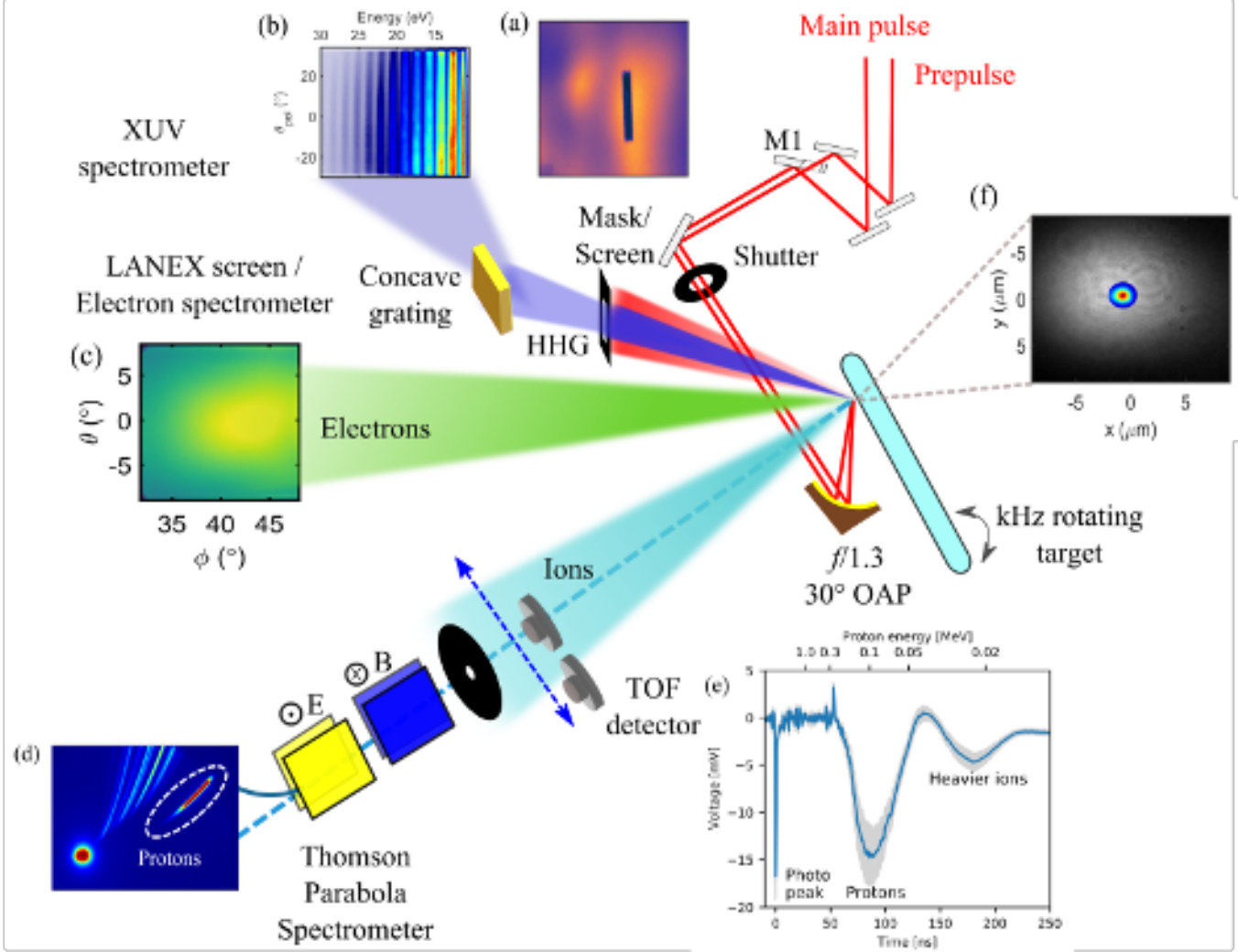
(b)
Energy (eV)
30 25 20 15
20
0
-20
(a)
Main pulse
Prepulse
M1
XUV
spectrometer
Mask/
Screen
Shutter
(f)
LANEX screen /
Electron spectrometer
Concave
grating
HHG
(c)
5
0
-5
θ (°)
35 40 45
ϕ (°)
Electrons
y (μm)
x (μm)
kHz rotating
target
f/1.3
30° OAP
Ions
B
E
TOF
detector
(e)
Proton energy (MeV)
1.0 0.3 0.1 0.05 0.02
Voltage (mV)
Heavier ions
Photo
peak
Protons
Time (ns)
(d)
Protons
Thomson
Parabola
Spectrometer

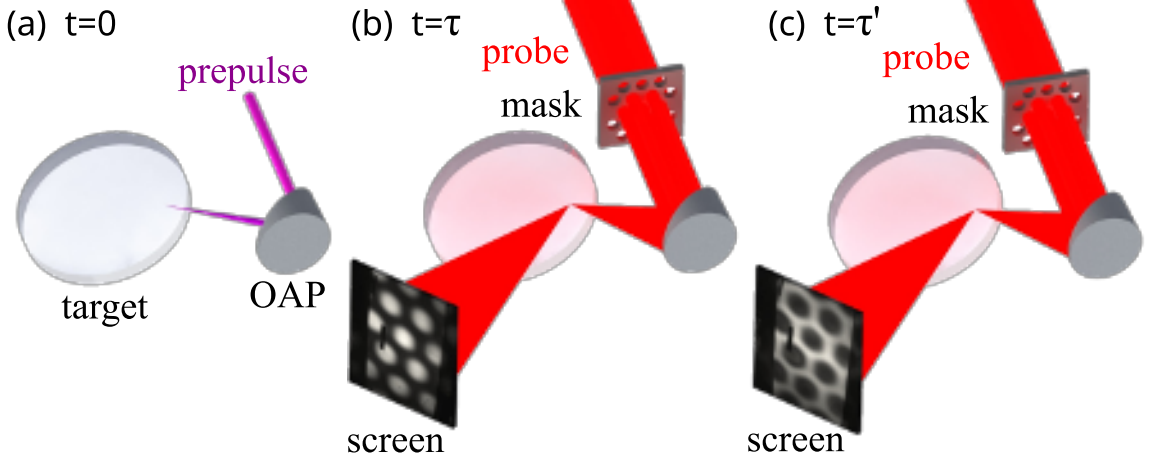
(a) t=0
prepulse
target
OAP
(b) t=τ
probe
mask
screen
(c) t=τ'
probe
mask
screen

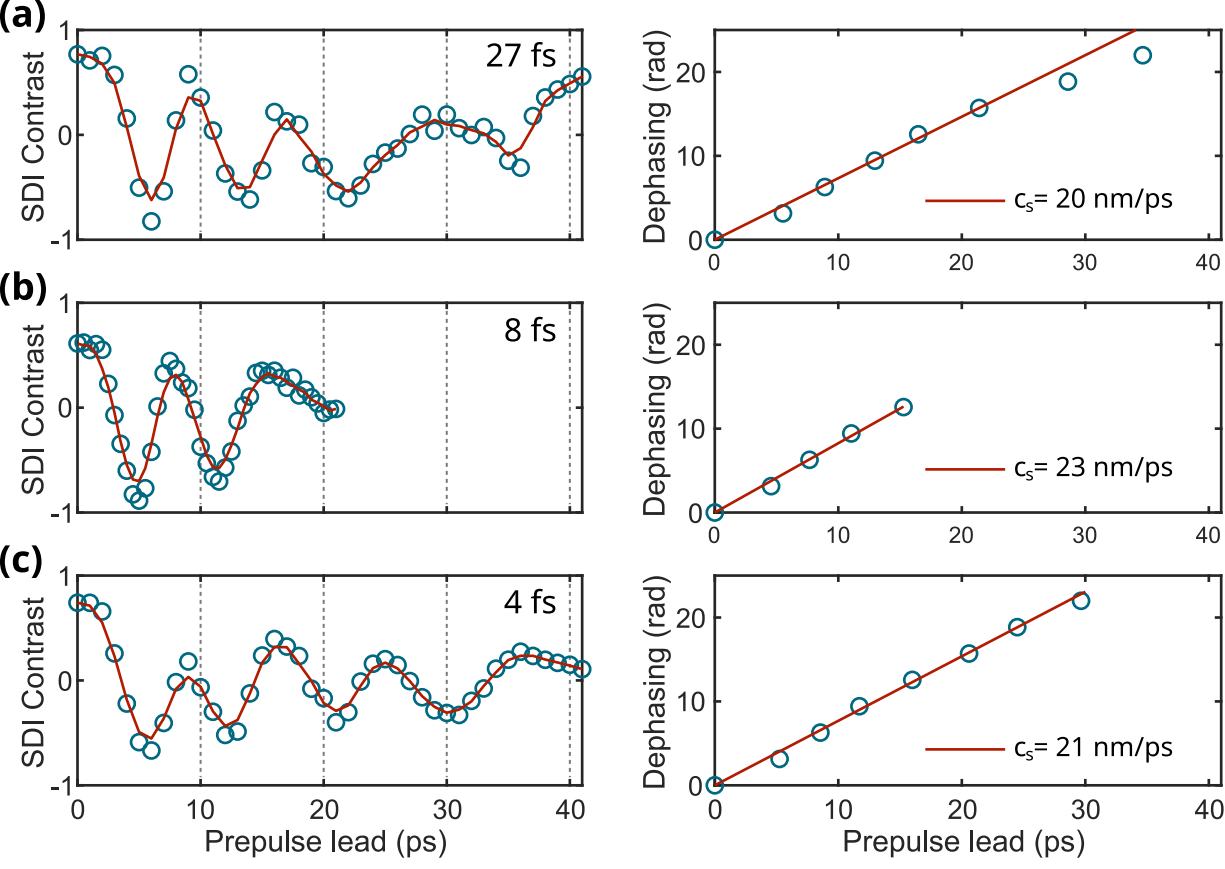
(a)
SDI Contrast
27 fs
Dephasing (rad)
c_s= 20 nm/ps
(b)
SDI Contrast
8 fs
Dephasing (rad)
c_s= 23 nm/ps
(c)
SDI Contrast
4 fs
Dephasing (rad)
c_s= 21 nm/ps
Prepulse lead (ps)
Prepulse lead (ps)

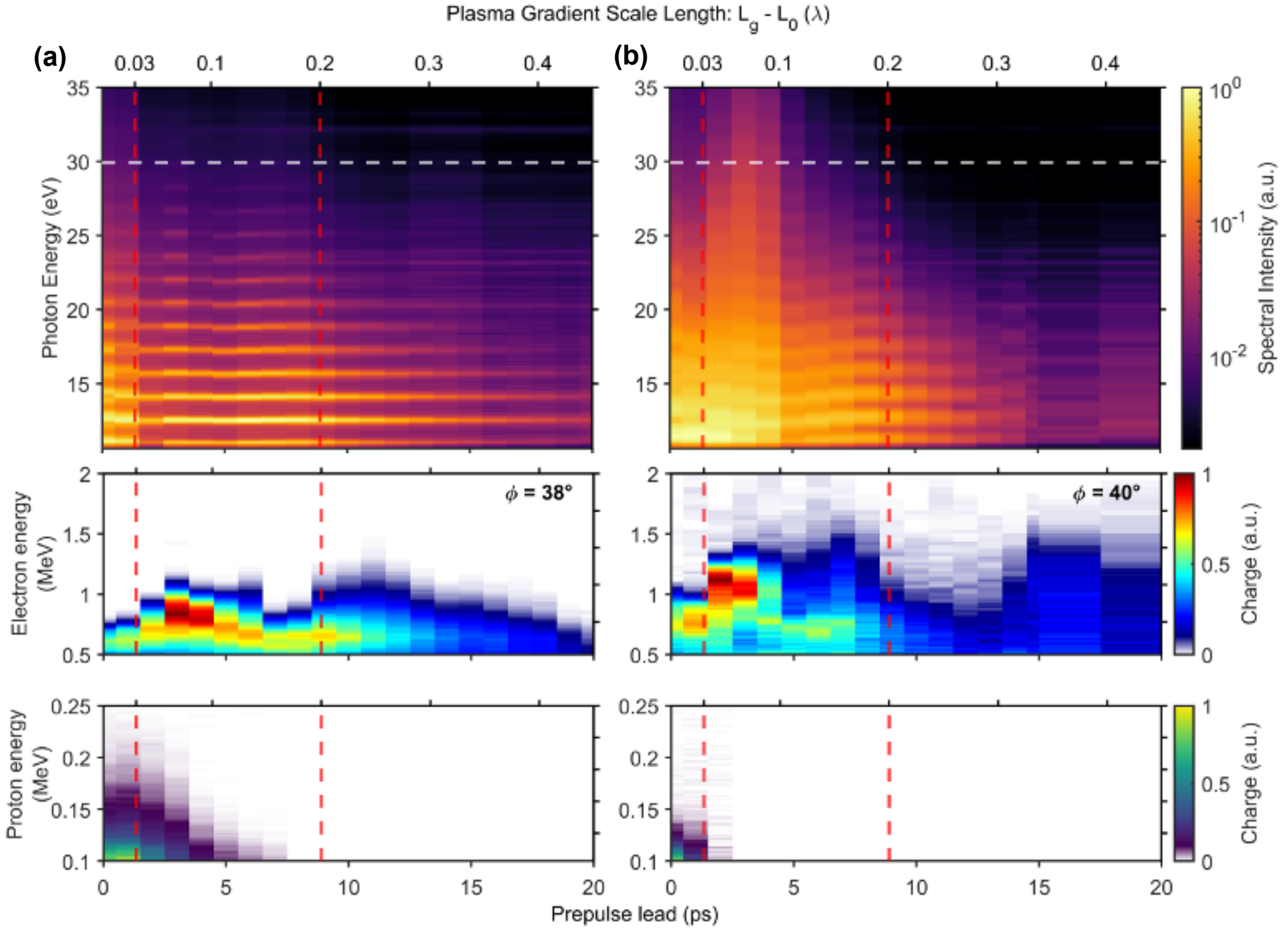
Plasma Gradient Scale Length: L_g - L_0 (λ)
(a)
(b)
0.03
0.1
0.2
0.3
0.4
Photon Energy (eV)
Spectral Intensity (a.u.)
Electron energy (MeV)
ϕ = 38°
ϕ = 40°
Charge (a.u.)
Proton energy (MeV)
Prepulse lead (ps)

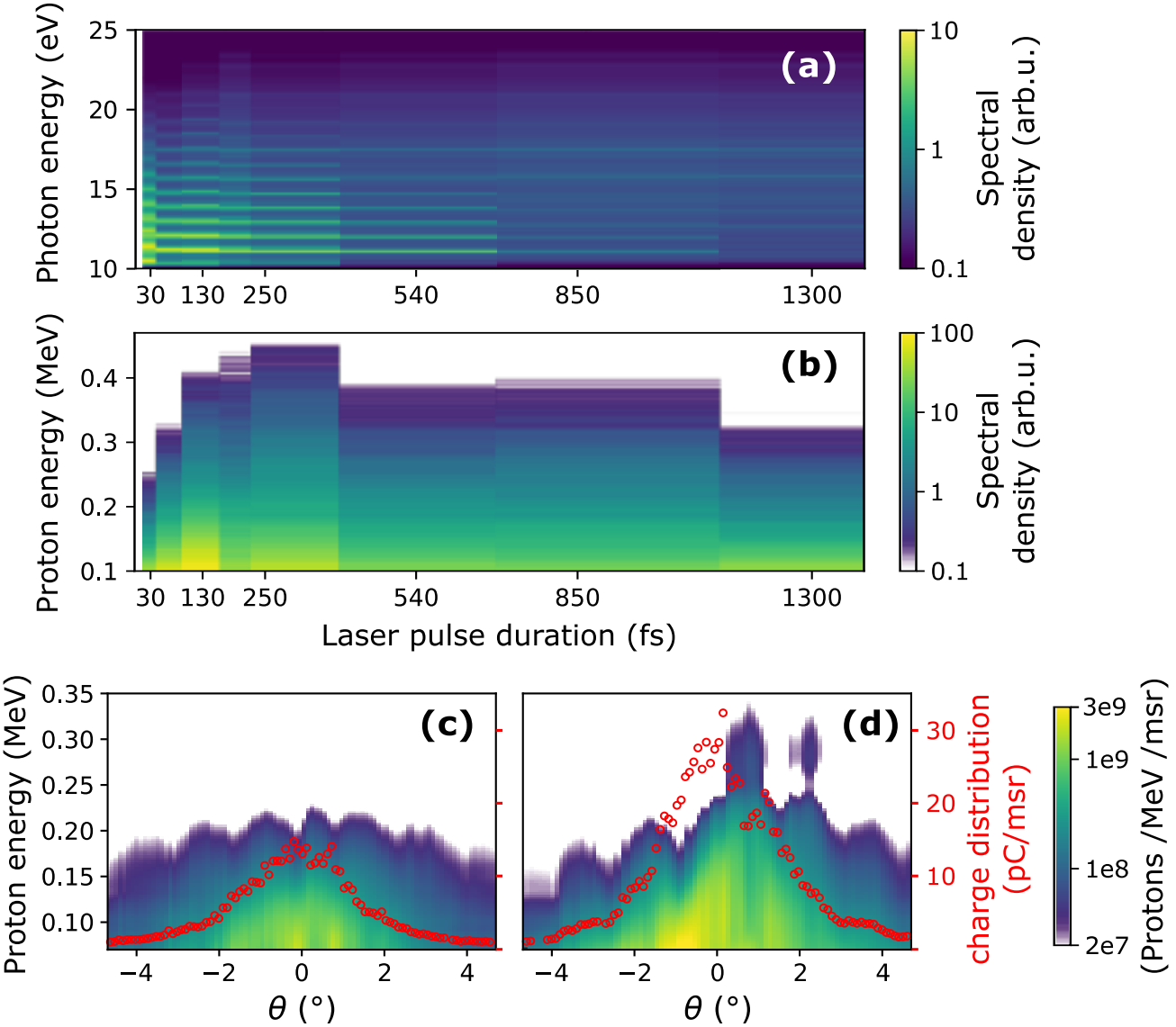
(a)
Photon energy (eV)
25
20
15
10
30 130 250 540 850 1300
10
1
0.1
Spectral density (arb.u.)
(b)
Proton energy (MeV)
0.4
0.3
0.2
0.1
30 130 250 540 850 1300
Laser pulse duration (fs)
100
10
1
0.1
Spectral density (arb.u.)
(c)
(d)
Proton energy (MeV)
0.35
0.30
0.25
0.20
0.15
0.10
−4 −2 0 2 4
θ (°)
charge distribution (pC/msr)
30
20
10
3e9
1e9
1e8
2e7
(Protons /MeV /msr)

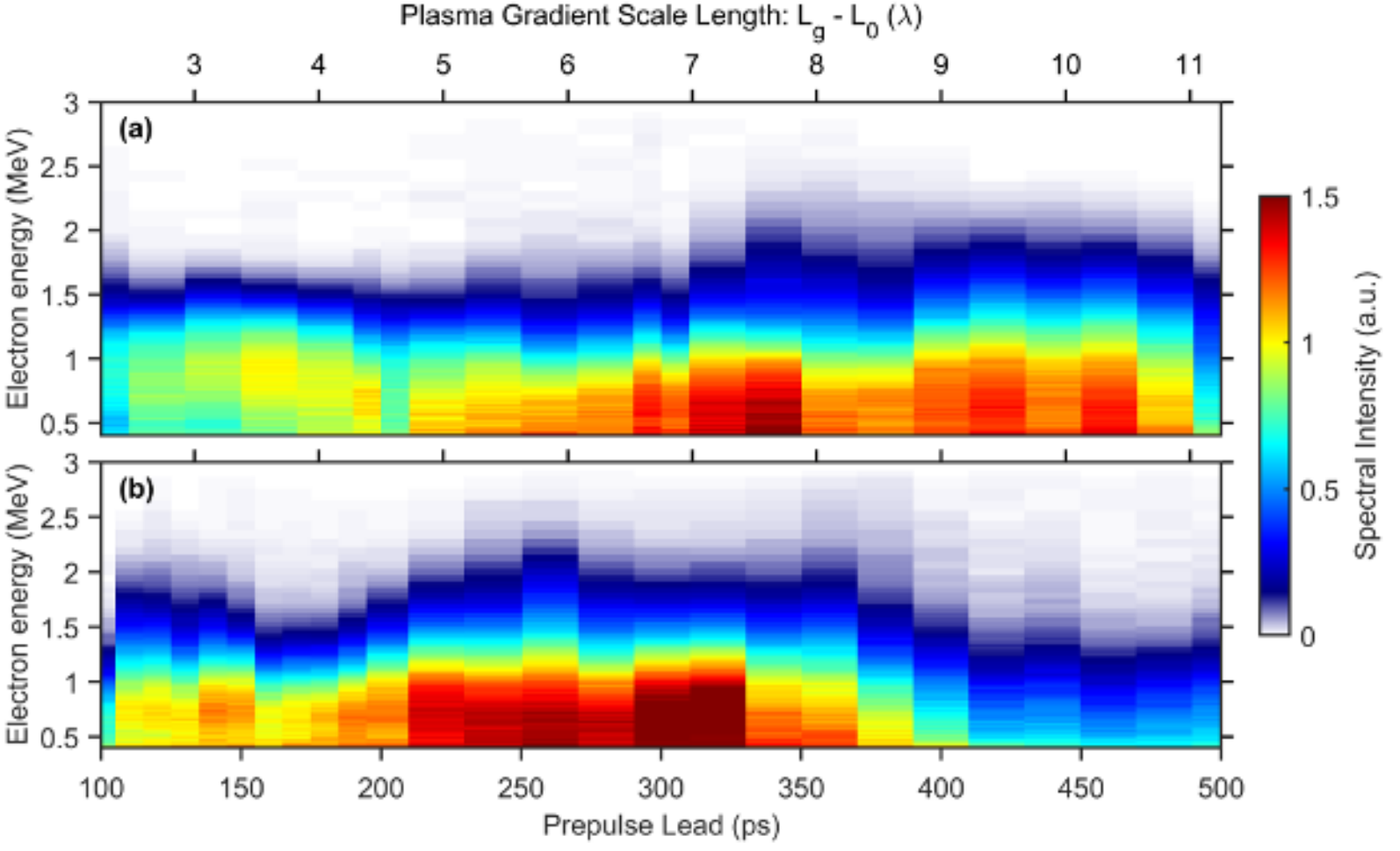
Plasma Gradient Scale Length: L_g - L_0 (λ)
3
4
5
6
7
8
9
10
11
(a)
(b)
Electron energy (MeV)
3
2.5
2
1.5
1
0.5
Spectral Intensity (a.u.)
1.5
1
0.5
0
100
150
200
250
300
350
400
450
500
Prepulse Lead (ps)